Dalton Transactions

PAPER

View Article Online
View Journal | View Issue

Cite this: *Dalton Trans.*, 2023, **52**, 2988

3D printing of cellulose/leaf-like zeolitic imidazolate frameworks (CelloZIF-L) for adsorption of carbon dioxide (CO_2) and heavy metal ions†

Hani Nasser Abdelhamid, *[a,b,c] Sahar Sultan[a] and Aji P. Mathew *[a]

Received 30th December 2022,
Accepted 6th February 2023

DOI: 10.1039/d2dt04168e

rsc.li/dalton

Metal–organic frameworks (MOFs) have advanced several technologies. However, it is difficult to market MOFs without processing them into a commercialized structure, causing an unnecessary delay in the material's use. Herein, three-dimensional (3D) printing of cellulose/leaf-like zeolitic imidazolate frameworks (ZIF-L), denoted as CelloZIF-L, is reported *via* direct ink writing (DIW, robocasting). Formulating CelloZIF-L into 3D objects can dramatically affect the material's properties and, consequently, its adsorption efficiency. The 3D printing process of CelloZIF-L is simple and can be applied *via* direct printing into a solution of calcium chloride. The synthesis procedure enables the formation of CelloZIF-L with a ZIF content of 84%. 3D printing enables the integration of macroscopic assembly with microscopic properties, *i.e.*, the formation of the hierarchical structure of CelloZIF-L with different shapes, such as cubes and filaments, with 84% loading of ZIF-L. The materials adsorb carbon dioxide (CO_2) and heavy metals. 3D CelloZIF-L exhibited a CO_2 adsorption capacity of 0.64–1.15 mmol g^{-1} at 1 bar (0 °C). The materials showed Cu^{2+} adsorption capacities of 389.8 ± 14–554.8 ± 15 mg g^{-1}. They displayed selectivities of 86.8%, 6.7%, 2.4%, 0.93%, 0.61%, and 0.19% toward Fe^{3+}, Al^{3+}, Co^{2+}, Cu^{2+}, Na^+, and Ca^{2+}, respectively. The simple 3D printing procedure and the high adsorption efficiencies reveal the promising potential of our materials for industrial applications.

Introduction

Three-dimensional (3D) printing technologies have become cheaper, and one can find suitable 3D printers for less than €500.[1–4] They have advanced several applications, including biomedical applications,[5] regenerative medicine,[6,7] tissue engineering,[8–10] wound healing,[11] photocatalysis,[12] and water treatment.[13] 3D printing can be achieved *via* several methods including fused deposition modeling (FDM) printing[1] and direct ink writing (DIW or robocasting).[14] Among several 3D printing methods, DIW is easy, simple, and can proceed at ambient temperature, offering a high potential for printing thermally unstable materials. DIW relies on the 3D printing ink extruded using a simple paste extrusion nozzle. However, forming printable ink is a tedious task in this approach. The ink requires the presence of a binder and support to improve the mechanical and printing properties of the materials to be printed. Among these additives, biopolymers *e.g.* cellulose-based derivatives advanced 3D bio-printing.[7,10,15] Biopolymers enable good printing properties.[16,17]

Metal–organic frameworks (MOFs) are promising porous materials for several applications.[18–24] 3D printed MOF monoliths were reported using a variety of supports,[4,25–28] including MOF-74,[29] the University of Texas at San Antonio-16 (UTSA-16),[30] Hong Kong University of Science and Technology (HKUST-1),[31] leaf-like zeolitic imidazolate frameworks (ZIF-L),[32] and ZIF-8.[33–36] This advanced the shaping and processing of MOF materials.[37] 3D printing offers the processing of the materials into a hierarchical structure with tunable properties.[4] It led to the formation of tunable porous structures between the crystals of MOFs that also offer tunable hierarchical porosity. 3D printed materials advanced MOF applications in several fields, such as water treatment.[16,38,39] However, 3D printing *via* FDM requires fabricating filaments that require several chemical steps.[40] On the other side, DIW is simple if the ink formation becomes easy.[41]

[a]Division of Materials and Environmental Chemistry, Stockholm University, Svante Arrhenius väg 16 C, Stockholm, SE-10691, Sweden.
E-mail: hany.abdelhamid@aun.edu.eg, aji.mathew@mmk.su.se
[b]Advanced Multifunctional Materials Laboratory, Department of Chemistry, Faculty of Science, Assiut University, Assiut, 71515, Egypt
[c]Nanotechnology Research Centre (NTRC), The British University in Egypt (BUE), El-Shorouk City, Suez Desert Road, P.O. Box 43, Cairo 11837, Egypt

†Electronic supplementary information (ESI) available. See DOI: **https://doi.org/10.1039/d2dt04168e**

Water contamination due to numerous pollutants limits drinking water resources. The World Health Organization (WHO) estimated that 5.8 billion people have no access to drinkable water. About 74% of the global population used a safely managed drinking-water service. Two million tons of industrial effluents and sewage are released into water, causing the death of 14 000 people every day. Among different pollutants, heavy metals are serious contaminants. One hundred forty million people from 50 countries drink water containing heavy metals that exceed the levels recommended by the WHO guidelines.[42] Detection and removal of heavy metals *via* adsorption are vital for water treatment.[43–49]

Greenhouse gases such as carbon dioxide (CO_2) are some of the main causes responsible for global warming.[50,51] In June 2021, the global atmospheric CO_2 reached 416 ppm representing a 1.5 times higher concentration than that measured in 1780.[50] Intergovernmental Panel on Climate Change (IPCC) expected that the atmospheric concentration of CO_2 will be increased from 400 ppm to 950 ppm from 2019 to 2100 (https://www.ipcc.ch/). Removal of CO_2 *via* capture and storage can reduce the concentration levels by 30–60% of those measured in 2000 by 2050.[51] Thus, several methods were reported for CO_2 removal *via* adsorption and catalysis.[52] Among several adsorbents, ZIF materials are promising for CO_2 removal offering high adsorption efficiency and good selectivity.

Herein, we reported a simple DIW method for 3D printing cellulose\ZIF-L (denoted as CelloZIF-L) using sodium alginate/$CaCl_2$. The procedure involved a one-pot synthesis of CelloZIF-L ink that can be 3D printed into porous cubes *via* a printer. The ink can also be used for DIW into a filament *via* soaking in a solution of $CaCl_2$. The materials were characterized using powder X-ray diffraction (PXRD), transmission electron microscopy (TEM), scanning electron microscopy (SEM), energy dispersive X-ray (EDX) analysis\mapping, nitrogen sorption isotherms, and thermogravimetric analysis (TGA). The materials were used for CO_2 capture and heavy metal (Fe^{3+}, Al^{3+}, Co^{2+}, Cu^{2+}, Na^{+}, and Ca^{2+}) adsorption. They exhibited high adsorption efficiency, good recyclability, and excellent selectivity.

Experimental

Materials and methods

Zinc nitrate hexahydrate ($Zn(NO_3)_2 \cdot 6H_2O$), copper sulfate ($CuSO_4$), ferric chloride ($FeCl_3$), aluminum chloride ($AlCl_3$), cobalt nitrate hexahydrate ($Co(NO_3)_2 \cdot 6H_2O$), 2-methyl imidazole (Hmim), sodium hydroxide (NaOH), sodium alginate, and calcium chloride ($CaCl_2$) were purchased from Sigma-Aldrich (Germany). The synthesis method in ref. 12 was used to synthesize TEMPO-oxidized cellulose nanofibers (TOCNF) using spruce cellulose pulp (Domsjö Fabriker AB, Sweden, never-dried form, 17 wt.%).

Ink preparation and 3D printing

ZIF-L was prepared *via* a one-pot method.[53,54] Typically, Zn $(NO_3)_2 \cdot 6H_2O$ (5 mmol, 1.5 g) was dispersed in TOCNF (100 mL, 1.5 wt.%) using an Ultra Turrax (IKA) at 15 000 rpm for one hour. NaOH (10 mL, one mmol) was then added dropwise with stirring. Finally, Hmim (50 mmol) was added. The mixture was mixed using an Ultra Turrax (15 000 rpm for 30 min). The material, *e.g.*, CelloZIF-L (63.6 wt.%), was then collected *via* centrifugation (10 000 rpm, 10 min, 20 °C). CelloZIF-L was then used to prepare the ink *via* mixing with sodium alginate (6 wt.%). The ink composition contains 67.64 g and 13.6 g of CelloZIF-L and sodium alginate per 100 mL of H_2O, respectively. It was then transferred to a syringe for printing. The ink was manually extruded several times (3–5) using different nozzles to make the ink printable.

Automatic 3D printing was performed using a Discov3ry Complete paste printing system (Structur3D Printing, https://www.structur3d.io, Ultimaker 2+, https://www.ultimaker.com). The printer was integrated with the Discov3ry Complete paste extruder. All printing procedures took place at room temperature (RT). The printed object was designed using a computer-aided design (CAD) model in '.stl' files that were converted to 'gcode' files for the printer. The printing process was achieved using an appropriate nozzle diameter of 410 µm (Movie 1, ESI†). It can be obtained using a flow rate and speed of 70–120% and 10–80 mm s^{-1}, respectively. The printing scaffolds were soaked in $CaCl_2$ (6 wt.%) for cross-linking with sodium alginate.

The direct printing into filament form was achieved via the direct addition of the ink to a solution of $CaCl_2$ (6 wt.%). The acquisition was performed by hand following the same printing conditions mentioned above. After printing *via* an automatic 3D printer or direct ink writing as cubes or filaments, the materials were labeled 3D CelloZIF-L_cubes and CelloZIF-L_filament, respectively.

The water in the printed materials was removed *via* freeze-drying (laboratory freeze dryer, ALPHA 1–2 Ldplus, Martin Christ, Germany). The dried materials were used for characterization and applications in adsorption.

Characterization

The material's crystallinity and phase purity were assessed using X-ray diffraction (PXRD, PANalytical X'Pert PRO X-ray diffractometer, Cu $K_{\alpha 1}$ radiation). The particle's size or morphology was evaluated using transmission electron microscopy (TEM, JEM 2100, JEOL, Japan, 200 kV) and scanning electron microscopy (SEM, TM3000 TableTop SEM, Hitachi, Japan, accelerating voltage 2–15 kV). Using the same SEM microscopy, the materials' composition and elemental distribution before and after metal ion adsorption were determined using energy-dispersive X-ray spectroscopy (EDX). The material's porosity was evaluated using nitrogen (N_2) adsorption–desorption isotherms (Micromeritics ASAP 2020 instrument, USA, 77K). The specific surface areas were determined using the Brunauer–Emmett–Teller (BET) method, the Langmuir model, and external surface area (using the t-plot method). The non-local density functional theory (NLDFT) method was applied to determine the pore size distribution using the model of N_2@77 on a carbon slit. Thermal stability and the ink's compositions were evaluated *via* thermogravimetric analysis (TGA, PerkinElmer TGA 7 thermal analyzer apparatus, Shimadzu, Japan, at a heating rate of 10 °C min^{-1} and an airflow rate of 30 mL min^{-1}).

Adsorption and desorption of carbon dioxide (CO_2)

The adsorption and desorption of CO_2 using the materials, *i.e.*, 3D cubes or filaments, were performed using a Micromeritics ASAP 2020 instrument (at 0 °C). The materials were degassed at 110 °C under reduced pressure for five hours before measurement using the degassing units of the same equipment. The adsorption–desorption process was performed to evaluate the recyclability using the same materials without any treatment during each run.

Metal adsorption

The adsorption of heavy metal ions was performed in an aqueous solution using a standard solution of metal ions (1000 ppm). Copper (Cu^{2+}) ions were tested to evaluate the material's performance for comparison. 3D CelloZIF-L_cubes and CelloZIF-L_filament (≈100 mg) were added to the Cu^{2+} ion solution (1000 ppm) for 24 h with shaking (400 rpm, RT). The effect of the initial concentration of the Cu^{2+} ion solution was evaluated using different Cu^{2+} ion solutions at 5, 10, 50, and 100 ppm following the same procedure. The materials were decanted and dried under vacuum (80 °C, 5 h) before visualization and analysis using SEM.

The selectivity of adsorption was examined using the same procedure mentioned above, except that heavy metals were mixed at the same concentration for elements such as Fe^{3+}, Al^{3+}, Co^{2+}, Ca^{2+}, and Na^{+}. Typically, 100 mg of each material was added to the mixed metal solutions (1000 ppm) before incubation for 12 h with shaking (400 rpm, 20 °C). The metal mapping and analysis were performed using EDX (SEM, TM3000 TableTop SEM, Hitachi, Japan, accelerating voltage 15 kV).

Results and discussion

Preparation of inks, printing, and materials characterization

The synthesis of cellulose-ZIF-L (CelloZIF-L) using TOCNF is schematically represented, as shown in Fig. 1. The procedure involved the successful addition of Zn^{2+}, OH^{-}, and Hmim in the presence of TOCNF (Fig. 1). The functional groups of TOCNF, *i.e.*, carboxylic and hydroxyl groups, ensure the coordination with Zn^{2+} that can be converted to zinc hydroxy nitrate nanosheets after adding OH^{-} (*i.e.*, NaOH). The phase formed during the successive addition of the chemicals was determined using PXRD (Fig. S1†). The PXRD patterns of the composite after adding NaOH to Zn^{2+}/TOCNF confirm the formation of zinc hydroxy nitrate nanosheets (Fig. S1†).[55] The crystal formation of ZIF-L was achieved after adding an organic linker, *i.e.*, Hmim, which led to the formation of CelloZIF-L inks. The inks were characterized using PXRD in a wet and dry state (Fig. S2†). The PXRD patterns of both cases confirm the successful formation of a pure phase of ZIF-L (Fig. S2†). The prepared inks were then used for 3D printing as cubes and filaments *via* automatic 3D printing and directly dropping into a solution of $CaCl_2$, respectively (Fig. 1).

The materials after printing were characterized using PXRD (Fig. 2a), TGA (Fig. 2b), nitrogen sorption isotherms (Fig. 2c and d), TEM images (Fig. 3), and SEM images (Fig. 4 and 5). The PXRD patterns of the printed cubes and filament agree with the simulated pattern of ZIF-L, indicating the successful formation of ZIF-L crystals in the printed objects (Fig. 2a). The diffraction pattern of TOCNF did not indicate a high content of ZIF-L inside the printed objects. The material compositions were further assessed using TGA (Fig. 2b). Thermal analysis using TGA of the ink shows a gradual weight loss (%) with a residual amount of 50% at 400 °C (Fig. 2b). The continuous weight loss in TGA for the ink is due to water losses and TOCNF. The mass residual of 50 wt.% at 400 °C refers to ZnO formed in the ink (Fig. 2b). The TGA curves for the printed cubes and filaments show thermal stability up to 600 °C (Fig. 2b). 3D CelloZIF-L_cubes and CelloZIF-L_filament display the same residual indicating the exact content of ZIF-L in both objects (Fig. 2b). They show ZnO residuals of 31–33%, corresponding to 84% ZIF-L. PXRD and TGA data analyses confirm the successful synthesis of CelloZIF-L with a high ZIF content (84%). The porosity of the 3D printed materials was evaluated using nitrogen sorption isotherms (Fig. 2c). The data analysis indicates that the BET and Langmuir specific surface areas, and the external surface area are 32, 50, and 22 m^2 g^{-1} for 3D CelloZIF-L_filament and 960, 1000, and

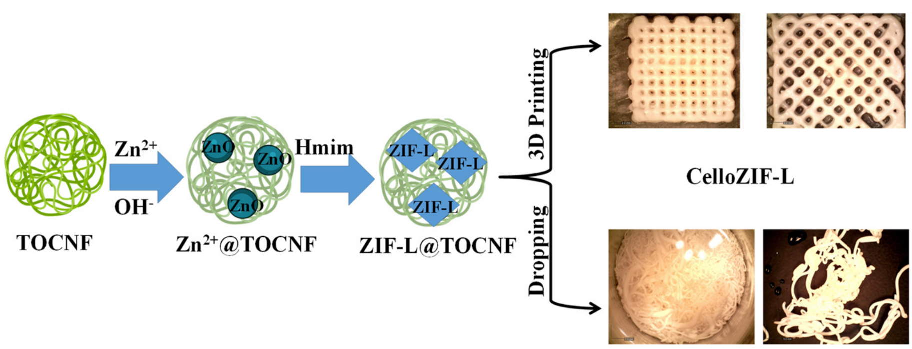

Fig. 1 Scheme for the *in situ* synthesis of ZIF-L in TOCNF and their processing into 3D cubes and filaments.

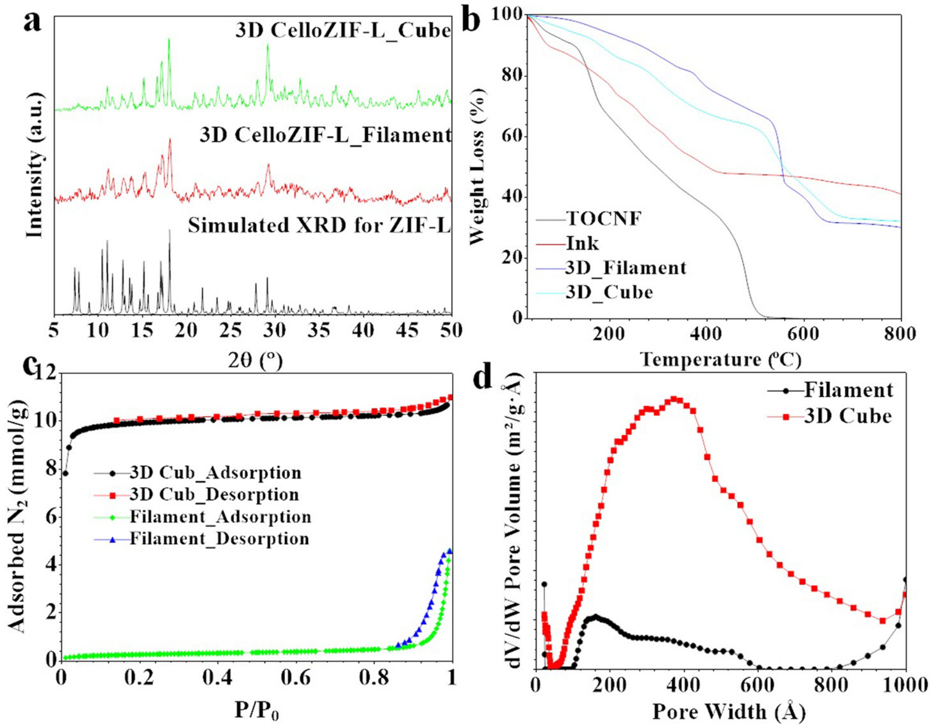

Fig. 2 Characterization of 3D printed objects using (a) PXRD, (b) TGA, (c) N_2 adsorption–desorption isotherms and (d) pore size distribution.

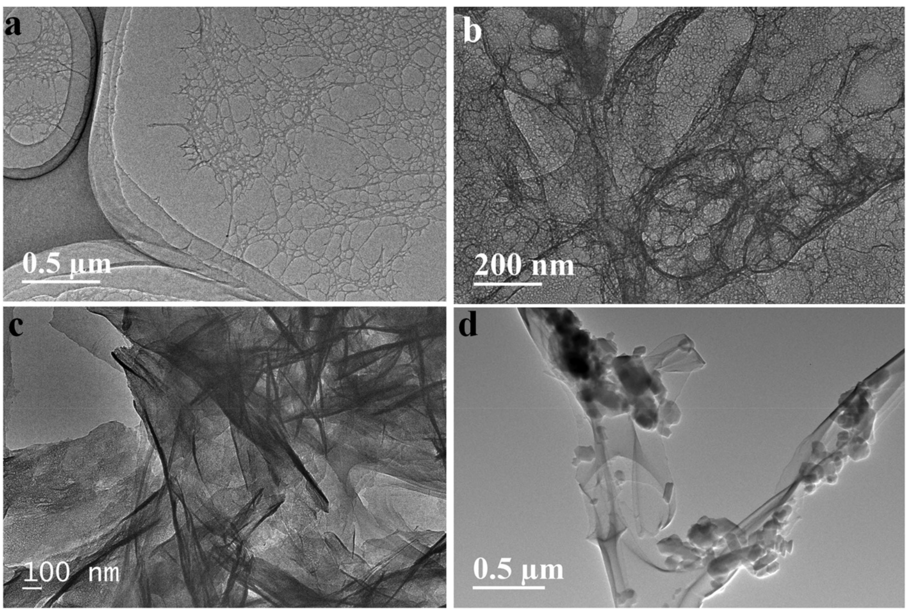

Fig. 3 TEM images of (a) TOCNF, (b) Zn^{2+}@TOCNF, (c) Zn/NaOH@TOCNF, and (d) ZIF-L@TOCNF.

125 m^2 g^{-1} for 3D CelloZIFL_cubes, respectively. The pore size distribution of the printed objects is characterized using DFT, as shown in Fig. 2d. The 3D CelloZIF-L_filament and 3D CelloZIFL_cubes show pore distributions of 10–60 nm and 10–90 nm, respectively (Fig. 2d). It is essential to mention that these pores are inside the crystals of ZIF-L.

The morphology of TOCNF, Zn^{2+}@TOCNF, ZnO@TOCNF, and ZIF-L@TOCNF was evaluated using TEM images (Fig. 3). The TEM image of TOCNF shows nanofibers with a diameter of 1–10 nm (Fig. 3a). The nanofibers tend to form a network due to the entangled properties of TOCNF *via* hydrogen bond interactions. The network is transparent after adding Zn^{2+} ions

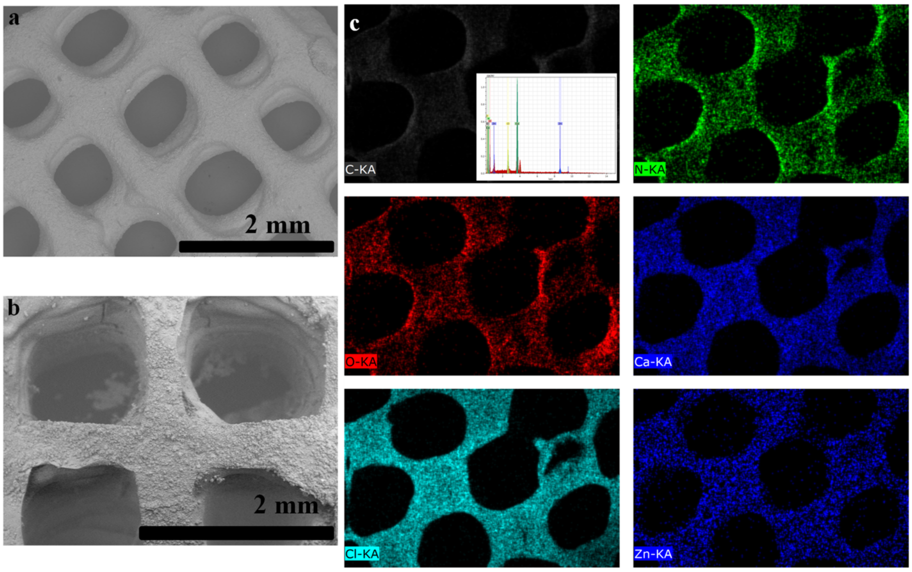

Fig. 4 (a and b) SEM images and (c) EDX analysis and mapping for 3D printing of CelloZIFL_cubes.

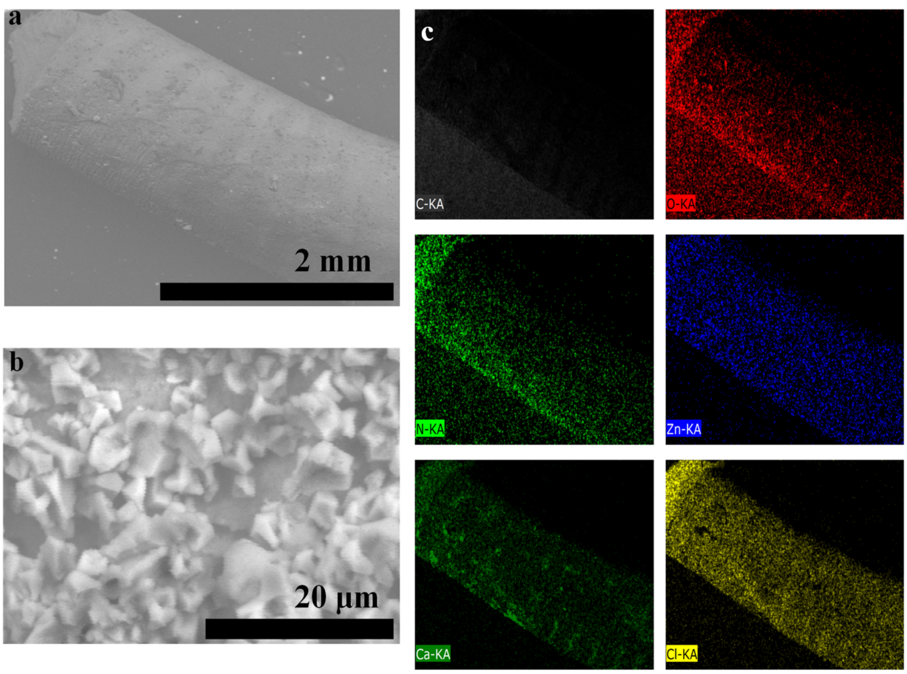

Fig. 5 (a and b) SEM images and (c) EDX analysis and mapping of CelloZIFL_filament.

that enabled coordination to the carboxylic groups of TOCNF (Fig. 3b). After adding NaOH, the coordinated Zn^{2+} inside TOCNF was converted to zinc nitrate nanosheets with a thickness of 10–50 nm (Fig. 3c). The formation of ZIF-L crystals was achieved after the addition of Hmim. The TEM image of the CelloZIF-L ink shows small crystals of 50–100 nm (Fig. 3d). The analysis of the TEM images confirms the integration of the ZIF-L crystals into the TOCNF network inside the CelloZIF-L ink (Fig. 3).

We evaluated the macropores of the printed objects using SEM images (Fig. 4). The 3D-printed objects were designed to have a 1 mm pore size (Fig. 1). The SEM images of 3D CelloZIF_cubes are shown in Fig. 4a and b. 3D CelloZIF_cubes display well-organized cubes with a pore size of 1 mm (Fig. 4a and b). The pore of the printed cubes is designed using CAD. Elemental analysis and mapping are performed using EDX analysis (Fig. 4c). The chemical composition shows C, O, N, Zn, Ca, and Cl elements. The distribution of Zn indicates that

ZIF-L is homogeneous, indicating the excellent dispersion of ZIF-L crystals inside the printed cubes (Fig. 4c).

The SEM image and EDX analysis/mapping of 3D CelloZIF-L_filament are shown in Fig. 5. The SEM images of the printed filaments show a diameter of 0.77 mm (Fig. 5a). The high magnification image displays the crystals of ZIF-L. Elemental analysis indicates the presence of C, O, N, Zn, Ca, and Cl (Fig. 5c). The heavy metal distribution of Zn shows the homogeneous distribution of ZIF-L in the formed filament (Fig. 5c).

3D printing *via* direct ink writing (DIW) offered several advantages. This method is easy without the need for a cumbersomely long fabrication time. Some previously reported methods require 15–120 h.[56] CelloZIF-L was printed without the need for extra agents such as gelatin. Calcium alginate/cellulose enabled 3D printing of ZIF-L without the need for other biopolymers such as gelatin[17] or inorganic binders such as Boehmite AlO(OH).[57] Our method is very cheap compared to other methods that require several chemical agents such as 2-phenoxy ethyl acrylate, trimethylolpropane triacrylate, bis (2,4,6-trimethyl benzoyl)-phenyl phosphine oxide, and 1-hydroxy-cyclohexyl-phenyl-ketone for single 3D printing procedures *via* photo-curation.[58]

CO_2 adsorption

The materials were evaluated for adsorption and desorption processes. 3D CelloZIF-L_cubes and 3D CelloZIF-L_filament were used for the adsorption of CO_2 (Fig. 6a). ZIF-L powder, 3D CelloZIF-L_cubes, and 3D CelloZIF-L_filament exhibit CO_2 adsorption capacities of 1.0, 1.15, and 0.64 mmol g^{-1}, respectively, at 1 bar at 0 °C (Fig. 6b). The cubes showed higher adsorption capacity than the filament. The high performance is due to the increased CO_2 diffusion inside the materials *via* the large pores of the 3D-printed objects with a pore size of 1 mm. There is no difference between the adsorption and desorption isotherms, indicating that the process is reversible.

The recyclability for CO_2 adsorption and desorption was also evaluated (Fig. 6c and d). 3D CelloZIF-L_cubes and 3D CelloZIF-L_filament can be used several times for CO_2 adsorption and desorption without a significant decrease in the material's performance, indicating the high recyclability of the materials. 3D CelloZIF-L_cubes and 3D CelloZIF-L_filament can be recycled for 4 and 3 runs of the adsorption and desorption processes, respectively (Fig. 6c and d).

The CO_2 adsorption of ZIF-L takes place *via* an open-gate mechanism.[59] The unique cushion-like cavities inside the leaf-like ZIF crystals enabled high CO_2 adsorption. The cushion-shaped cavity is flexible compared to excavating isoreticular materials such as ZIF-8 with a tetrahedral structure. The 2D morphology of ZIF-L exhibits a weak connection between terminal Hmim-4 and free Hmim-5 inside ZIF-L ($Zn(mim)_2\cdot(Hmim)_{1/2}\cdot(H_2O)_{3/2}$). 3D CelloZIF-L showed high adsorption performance for CO_2, offering promising application in gas removal filters.

The printed materials enable simple CO_2 capture with high adsorption capacities and excellent recyclability. 3D-printed ZIF-8 synthesized using ZIF-8 powder (Basolite 1200), bentonite, and methylcellulose has been reported.[33] The materials

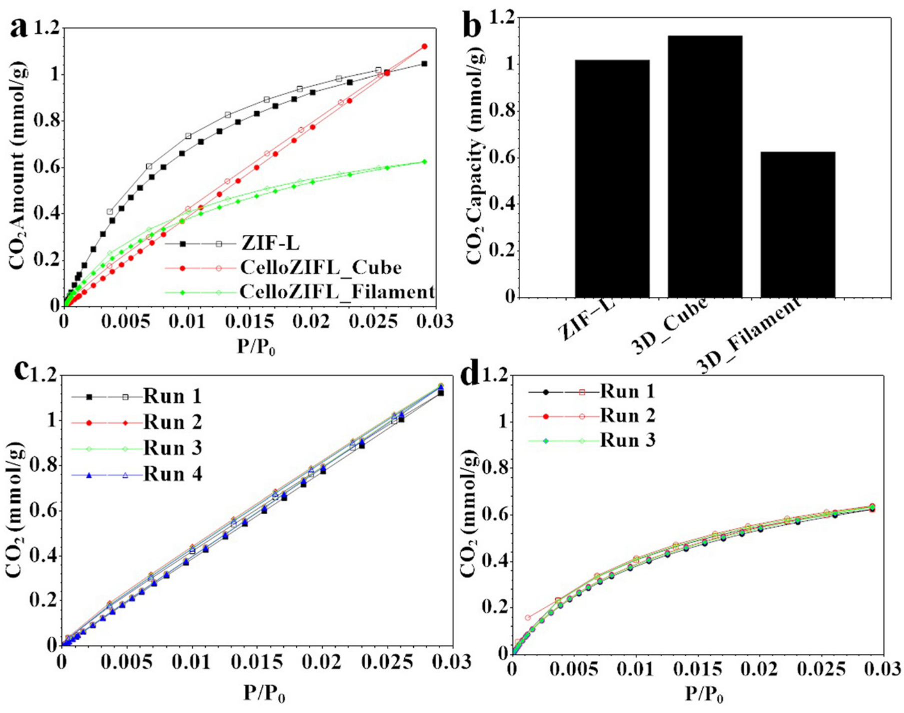

Fig. 6 (a) CO_2 adsorption–desorption isotherms, (b) CO_2 adsorption capacities, and (c and d) CO_2 recyclability of (c) 3D CelloZIF-L_cubes and (d) 3D CelloZIF-L_filament.

were mixed with water to form a printable ink. Methylcellulose was removed *via* activation under argon at 450 °C, giving a final composition of 80 wt.% and 20 wt.% of ZIF-8 and bentonite, respectively. The 3D printed ZIF was tested for CO_2 adsorption at 1 bar offering an adsorption capacity of 1.3 mmol g^{-1}, which was higher than that of ZIF-8 powder (CO_2 adsorption capacity of 0.82 mmol g^{-1}).[33] Data analysis also showed a separation factor of 4.1 for a mixture of 70 : 30 vol% : vol% of $CH_4 : CO_2$, which was higher than the reported value for ZIF-8 powder.[33]

Heavy metal adsorption

Copper (Cu^{2+}) ions were used as a model for heavy metal adsorption. Water treatment *via* the removal of heavy metal ions was tested for 3D CelloZIF-L_cubes and 3D CelloZIF-L_filament (Fig. 7). 3D CelloZIF-L_cubes exhibited higher adsorption of Cu^{2+} ions than 3D CelloZIF-L_filament (Fig. 7a). This observation has previously been reported for CO_2 adsorption, as shown in Fig. 6c and d. 3D CelloZIF-L_cubes and 3D CelloZIF-L_filament exhibited adsorption capacities of 554.8 ± 15 and 389.8 ± 14 mg g^{-1}, respectively (Fig. 7a).

The effect of Cu^{2+} ion initial concentration was evaluated, as shown in Fig. 7b. The Cu^{2+} initial concentrations of 5, 10, 50, and 100 mL (1000 ppm) show adsorption capacities of 223.7 ± 5, 554.8 ± 15, 585.8 ± 17, and 547.4 ± 16 mg g^{-1}, respectively (Fig. 7b). The adsorbed Cu^{2+} ions are homogeneously distributed at all tested concentrations (Fig. S3–S6†). The naked eye can confirm the adsorption based on the color change from white to turquoise blue (Fig. 7c and d). There is no change in the printed objects' dimension or porosity after the metal adsorption.

The selectivity of heavy metal adsorption is evaluated using a mixed metal solution containing several metal ions including trivalent (Fe^{3+} and Al^{3+}), divalent (Ca^{2+}, Cu^{2+}, and Co^{2+}), and monovalent ions (Na^+, Fig. 7e). 3D CelloZIF-L_cubes show selectivities of 86.8%, 6.7%, 2.4%, 0.93%, 0.61%, and 0.19% for Fe^{3+}, Al^{3+}, Co^{2+}, Cu^{2+}, Na^+, and Ca^{2+}, respectively (Fig. 7e). The same selectivity trend was observed for 3D CelloZIF-L_filament with selectivities of 93.5%, 2.2%, 3.5%, 0.18%, 0.52%, and 0.12% for Fe^{3+}, Al^{3+}, Co^{2+}, Cu^{2+}, Na^+, and Ca^{2+}, respectively (Fig. 7e). The high selectivity toward trivalent (Fe^{3+}) and divalent ions (Co^{2+} and Cu^{2+}) is due to TOCNF and ZIF-L, respectively. Hard metals such as Fe^{3+} ions tend to inter-

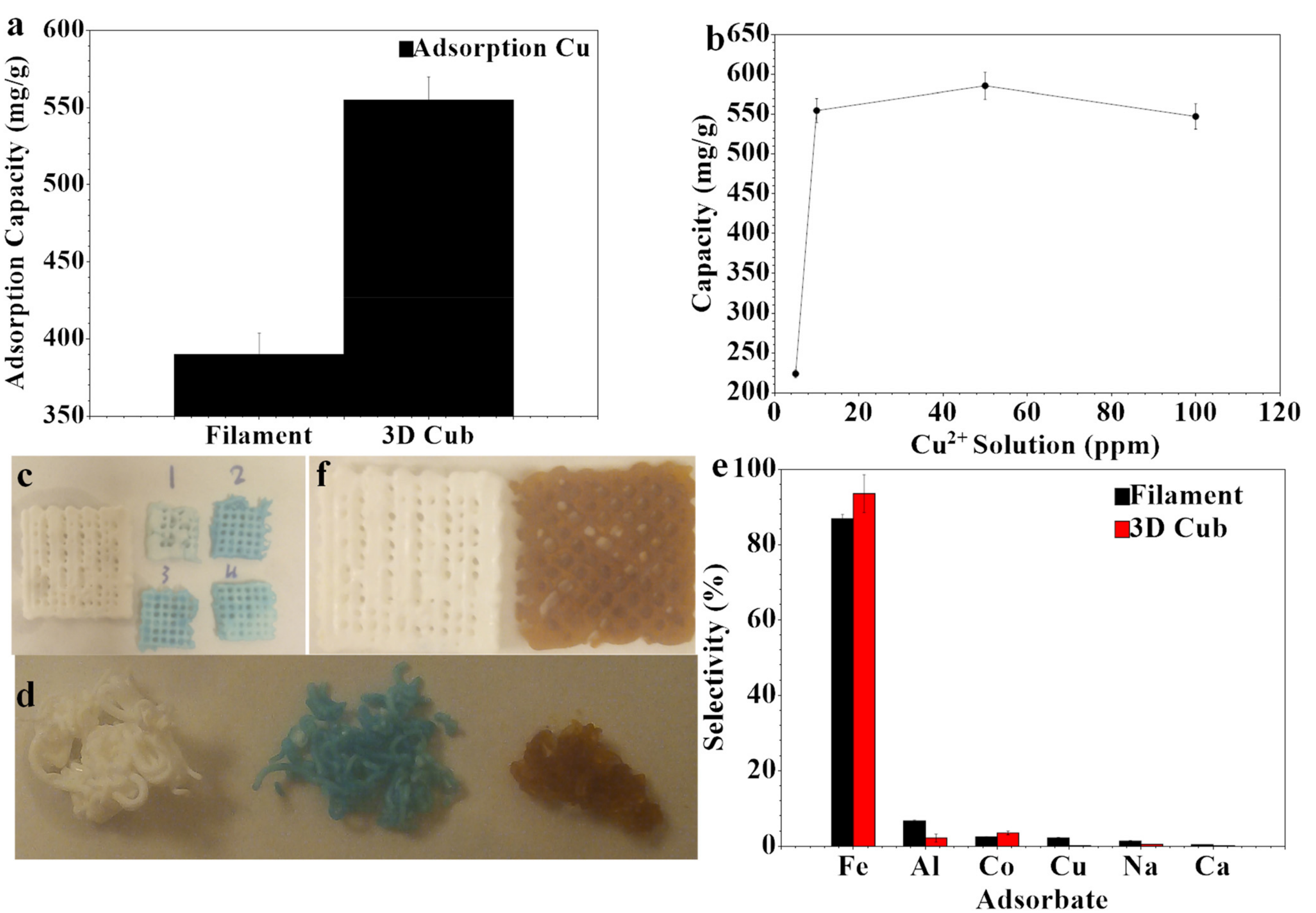

Fig. 7 (a) Adsorption capacity for Cu^{2+} ions of the 3D cubes and filament, (b) adsorption of Cu^{2+} ions using the 3D cubes with different initial concentrations, and (c) the cubes after adsorption of Cu^{2+} at (1) 5 ppm, (2) 10 ppm, (3) 50 ppm and (4) 100 ppm, (d and f) objects after adsorption of mixed metal ions, and (e) selectivity toward different metal ions.

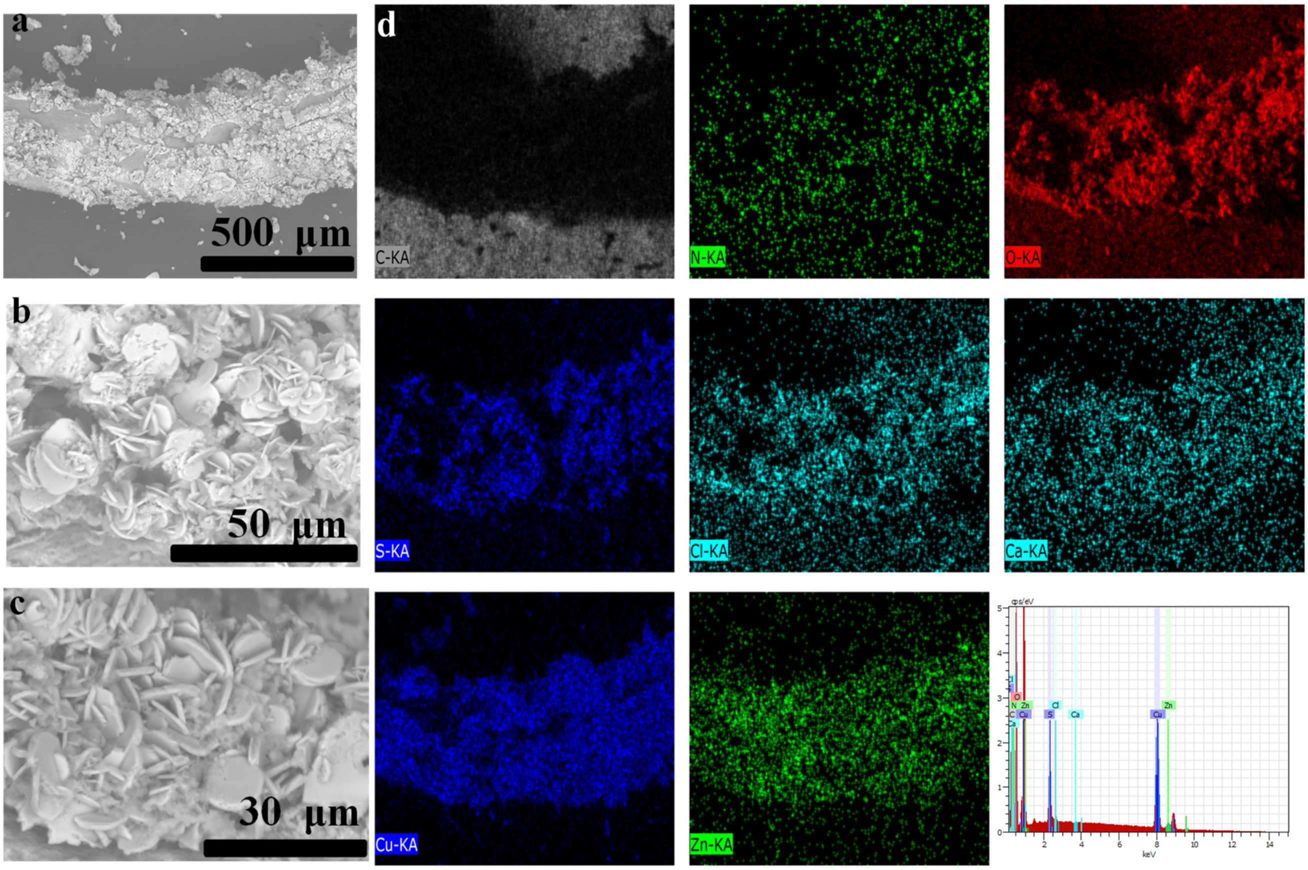

Fig. 8 (a–c) SEM images and (d) EDX analysis and mapping for the filament after the adsorption of Cu^{2+} ions.

act with the hydroxyl groups of TOCNF. At the same time, ZIF-L exhibits high selectivity towards copper ions.

The adsorption of Cu^{2+} ions on 3D CelloZIF-L_filament was characterized using SEM images, EDX analysis, and mapping (Fig. 8). The filament preserves its morphology after the adsorption. The SEM image of Cu^{2+}-adsorbed 3D CelloZIF-L_filament shows the leaf-like morphology of ZIF-L crystals (Fig. 8a–c). The observed plate shows particles with a thickness of 100–300 nm (Fig. 8c). This observation indicates that the adsorbed Cu^{2+} ions exhibit no change in the morphology of the ZIF-L crystals. EDX analysis and mapping confirm the presence of Zn and Cu, indicating Cu's adsorption on the filament (Fig. 8d). Based on the distribution of Cu, the adsorbed species are homogeneously distributed on the filament (Fig. 8c).

Conclusion

A simple 3D printing *via* direct ink writing (DIW) for TOCNF \ZIF-L\sodium alginate was presented. The materials obtained using a one-pot method provided printable inks for robocasting and the hand-made printing procedure. A high loading *i.e.* 84% of ZIF-L can be achieved using this procedure. The materials can be used as efficient adsorbents for CO_2 and heavy metal ions. They exhibited high adsorption capacities, good recyclability, and excellent selectivity. The simple ink formation and 3D printing procedure indicate that our method has the potential for large-scale production.

Conflicts of interest

There are no conflicts to declare.

Acknowledgements

This project is funded by The Swedish Foundation for Strategic Environmental Research (Mistra), MISTRA TerraClean (project no. 2015/31).

References

1 V. Saggiomo, A 3D Printer in the Lab: Not Only a Toy, *Adv. Sci.*, 2022, 2202610, DOI: 10.1002/advs.202202610.
2 M. L. Bedell, A. M. Navara, Y. Du, S. Zhang and A. G. Mikos, Polymeric Systems for Bioprinting, *Chem. Rev.*, 2020, **120**(19), 10744–10792, DOI: 10.1021/acs.chemrev.9b00834.

3 S. Heid and A. R. Boccaccini, Advancing Bioinks for 3D Bioprinting Using Reactive Fillers: A Review, *Acta Biomater.*, 2020, **113**, 1–22, DOI: **10.1016/j.actbio.2020.06.040**.
4 W. Y. Lieu, D. Fang, K. J. Tay, X. L. Li, W. C. Chu, Y. S. Ang, D. Li, L. Ang, Y. Wang and H. Y. Yang, Progress on 3D–Printed Metal–Organic Frameworks with Hierarchical Structures, *Adv. Mater. Technol.*, 2022, 2200023, DOI: **10.1002/admt.202200023**.
5 L. R. R. da Silva, W. F. Sales, F. d. A. R. Campos, J. A. G. de Sousa, R. Davis, A. Singh, R. T. Coelho and B. Borgohain, A Comprehensive Review on Additive Manufacturing of Medical Devices, *Prog. Addit. Manuf.*, 2021, **6**(3), 517–553, DOI: **10.1007/s40964-021-00188-0**.
6 C. Li and W. Cui, 3D Bioprinting of Cell-Laden Constructs for Regenerative Medicine, *Eng. Regen.*, 2021, **2**, 195–205, DOI: **10.1016/j.engreg.2021.11.005**.
7 X. Yang, S. Li, Y. Ren, L. Qiang, Y. Liu, J. Wang and K. Dai, 3D Printed Hydrogel for Articular Cartilage Regeneration, *Composites, Part B*, 2022, **237**, 109863, DOI: **10.1016/j.compositesb.2022.109863**.
8 E. Dogan, A. Bhusal, B. Cecen and A. K. Miri, 3D Printing Metamaterials towards Tissue Engineering, *Appl. Mater. Today*, 2020, **20**, 100752, DOI: **10.1016/j.apmt.2020.100752**.
9 S. Vanaei, M. S. Parizi, S. Vanaei, F. Salemizadehparizi and H. R. Vanaei, An Overview on Materials and Techniques in 3D Bioprinting Toward Biomedical Application, *Eng. Regen.*, 2021, **2**, 1–18, DOI: **10.1016/j.engreg.2020.12.001**.
10 S. Chae and D.-W. Cho, Biomaterial-Based 3D Bioprinting Strategy for Orthopedic Tissue Engineering, *Acta Biomater.*, 2022, **156**, 4–20, DOI: **10.1016/j.actbio.2022.08.004**.
11 P. E. Antezana, S. Municoy, M. I. Álvarez-Echazú, P. L. Santo-Orihuela, P. N. Catalano, T. H. Al-Tel, F. B. Kadumudi, A. Dolatshahi-Pirouz, G. Orive and M. F. Desimone, The 3D Bioprinted Scaffolds for Wound Healing, *Pharmaceutics*, 2022, **14**(2), 464, DOI: **10.3390/pharmaceutics14020464**.
12 N. Li, K. Tong, L. Yang and X. Du, Review of 3D Printing in Photocatalytic Substrates and Catalysts, *Mater. Today Energy*, 2022, **29**, 101100, DOI: **10.1016/j.mtener.2022.101100**.
13 D. Saidulu, A. Srivastava and A. K. Gupta, Enhancement of Wastewater Treatment Performance Using 3D Printed Structures: A Major Focus on Material Composition, Performance, Challenges, and Sustainable Assessment, *J. Environ. Manage.*, 2022, **306**, 114461, DOI: **10.1016/j.jenvman.2022.114461**.
14 S. Lawson, A.-A. Alwakwak, A. A. Rownaghi and F. Rezaei, Gel–Print–Grow: A New Way of 3D Printing Metal–Organic Frameworks, *ACS Appl. Mater. Interfaces*, 2020, **12**(50), 56108–56117, DOI: **10.1021/acsami.0c18720**.
15 D. M. Solis and A. Czekanski, 3D and 4D Additive Manufacturing Techniques for Vascular-like Structures – A Review, *Bioprinting*, 2022, **25**, e00182, DOI: **10.1016/j.bprint.2021.e00182**.
16 N. Li, D. Qiao, S. Zhao, Q. Lin, B. Zhang and F. Xie, 3D Printing to Innovate Biopolymer Materials for Demanding Applications: A Review, *Mater. Today Chem.*, 2021, **20**, 100459, DOI: **10.1016/j.mtchem.2021.100459**.
17 R. Pei, L. Fan, F. Zhao, J. Xiao, Y. Yang, A. Lai, S.-F. Zhou and G. Zhan, 3D-Printed Metal-Organic Frameworks within Biocompatible Polymers as Excellent Adsorbents for Organic Dyes Removal, *J. Hazard. Mater.*, 2020, **384**, 121418, DOI: **10.1016/j.jhazmat.2019.121418**.
18 J. Yao and H. Wang, Zeolitic Imidazolate Framework Composite Membranes and Thin Films: Synthesis and Applications, *Chem. Soc. Rev.*, 2014, **43**(13), 4470, DOI: **10.1039/c3cs60480b**.
19 O. Yassine, O. Shekhah, A. H. Assen, Y. Belmabkhout, K. N. Salama and M. Eddaoudi, H_2S Sensors: Fumarate-Based Fcu-MOF Thin Film Grown on a Capacitive Interdigitated Electrode, *Angew. Chem., Int. Ed.*, 2016, **55**(51), 15879–15883, DOI: **10.1002/anie.201608780**.
20 H.-C. Zhou, J. R. Long and O. M. Yaghi, Introduction to Metal–Organic Frameworks, *Chem. Rev.*, 2012, **112**(2), 673–674, DOI: **10.1021/cr300014x**.
21 L. E. Kreno, K. Leong, O. K. Farha, M. Allendorf, R. P. Van Duyne and J. T. Hupp, Metal-Organic Framework Materials as Chemical Sensors, *Chem. Rev.*, 2012, **112**(2), 1105–1125, DOI: **10.1021/cr200324t**.
22 Y. Wu, Y. Li, T. Zhao, X. Wang, V. I. Isaeva, L. M. Kustov, J. Yao and J. Gao, Bimetal-Organic Framework-Derived Nanotube@cellulose Aerogels for Peroxymonosulfate (PMS) Activation, *Carbohydr. Polym.*, 2022, **296**, 119969, DOI: **10.1016/j.carbpol.2022.119969**.
23 H. N. Abdelhamid, M. Wilk-Kozubek, A. M. El-Zohry, A. Bermejo Gómez, A. Valiente, B. Martín-Matute, A. V. Mudring and X. Zou, Luminescence Properties of a Family of Lanthanide Metal-Organic Frameworks, *Microporous Mesoporous Mater.*, 2019, **279**, 400–406, DOI: **10.1016/j.micromeso.2019.01.024**.
24 H. M. El-Bery and H. N. Abdelhamid, Photocatalytic Hydrogen Generation via Water Splitting Using ZIF-67 Derived Co_3O_4@C/TiO_2, *J. Environ. Chem. Eng.*, 2021, **9**(4), 105702, DOI: **10.1016/j.jece.2021.105702**.
25 X. Qi, K. Liu and Z. Chang, Beyond Powders: Monoliths on the Basis of Metal-Organic Frameworks (MOFs), *Chem. Eng. J.*, 2022, **441**, 135953, DOI: **10.1016/j.cej.2022.135953**.
26 B. Yeskendir, J.-P. Dacquin, Y. Lorgouilloux, C. Courtois, S. Royer and J. Dhainaut, From Metal–Organic Framework Powders to Shaped Solids: Recent Developments and Challenges, *Mater. Adv.*, 2021, **2**(22), 7139–7186, DOI: **10.1039/D1MA00630D**.
27 D. Liu, P. Jiang, X. Wang and W. Liu, *Additively Manufacturing Metal–Organic Frameworks and Derivatives: Methods, Functional Objects, and Applications*, 2021, pp. 17–51. DOI: **10.1021/bk-2021-1393.ch002**.
28 N. Maldonado and P. Amo-Ochoa, New Promises and Opportunities in 3D Printable Inks Based on Coordination Compounds for the Creation of Objects with Multiple Applications, *Chem. – Eur. J.*, 2021, **27**(9), 2887–2907, DOI: **10.1002/chem.202002259**.

29 S. Lawson, M. Snarzyk, D. Hanify, A. A. Rownaghi and F. Rezaei, Development of 3D-Printed Polymer-MOF Monoliths for CO 2 Adsorption, *Ind. Eng. Chem. Res.*, 2020, **59**(15), 7151–7160, DOI: 10.1021/acs.iecr.9b05445.

30 S. Lawson, Q. Al-Naddaf, A. Krishnamurthy, M. S. Amour, C. Griffin, A. A. Rownaghi, J. C. Knox and F. Rezaei, UTSA-16 Growth within 3D-Printed Co-Kaolin Monoliths with High Selectivity for CO2\CH4, CO2/N2, and CO2/H2 Separation, *ACS Appl. Mater. Interfaces*, 2018, **10**(22), 19076–19086, DOI: 10.1021/acsami.8b05192.

31 A. K. Chaudhari, I. Han and J.-C. Tan, Multifunctional Supramolecular Hybrid Materials Constructed from Hierarchical Self-Ordering of In Situ Generated Metal-Organic Framework (MOF) Nanoparticles, *Adv. Mater.*, 2015, **27**(30), 4438–4446, DOI: 10.1002/adma.201501448.

32 S. Yuan, J. Zhu, Y. Li, Y. Zhao, J. Li, P. Van Puyvelde and B. Van der Bruggen, Structure Architecture of Micro/Nanoscale ZIF-L on a 3D Printed Membrane for a Superhydrophobic and Underwater Superoleophobic Surface, *J. Mater. Chem. A*, 2019, **7**(6), 2723–2729, DOI: 10.1039/C8TA10249J.

33 I. Pellejero, F. Almazán, M. Lafuente, M. A. Urbiztondo, M. Drobek, M. Bechelany, A. Julbe and L. M. Gandía, Functionalization of 3D Printed ABS Filters with MOF for Toxic Gas Removal, *J. Ind. Eng. Chem.*, 2020, **89**, 194–203, DOI: 10.1016/j.jiec.2020.05.013.

34 K. A. Evans, Z. C. Kennedy, B. W. Arey, J. F. Christ, H. T. Schaef, S. K. Nune and R. L. Erikson, Chemically Active, Porous 3D-Printed Thermoplastic Composites, *ACS Appl. Mater. Interfaces*, 2018, **10**(16), 15112–15121, DOI: 10.1021/acsami.7b17565.

35 B. Claessens, N. Dubois, J. Lefevere, S. Mullens, J. Cousin-Saint-Remi and J. F. M. Denayer, 3D-Printed ZIF-8 Monoliths for Biobutanol Recovery, *Ind. Eng. Chem. Res.*, 2020, **59**(18), 8813–8824, DOI: 10.1021/acs.iecr.0c00453.

36 B. Verougstraete, D. Schuddinck, J. Lefevere, G. V. Baron and J. F. M. Denayer, A 3D-Printed Zeolitic Imidazolate Framework-8 Monolith For Flue- and Biogas Separations by Adsorption: Influence of Flow Distribution and Process Parameters, *Front. Chem. Eng.*, 2020, **2**, 589686, DOI: 10.3389/fceng.2020.589686.

37 Z. Wang, L. Liu, Z. Li, N. Goyal, T. Du, J. He and G. K. Li, Shaping of Metal–Organic Frameworks: A Review, *Energy Fuels*, 2022, **36**(6), 2927–2944, DOI: 10.1021/acs.energyfuels.1c03426.

38 N. H. M. Yusoff, L.-R. I. Teo, S. J. Phang, V.-L. Wong, K. H. Cheah and S.-S. Lim, Recent Advances in Polymer-Based 3D Printing for Wastewater Treatment Application: An Overview, *Chem. Eng. J.*, 2022, **429**, 132311, DOI: 10.1016/j.cej.2021.132311.

39 P. Ghosal, B. Gupta, R. S. Ambekar, M. M. Rahman, P. M. Ajayan, N. Aich, A. K. Gupta and C. S. Tiwary, 3D Printed Materials in Water Treatment Applications, *Adv. Sustainable Syst.*, 2022, **6**(3), 2100282, DOI: 10.1002/adsu.202100282.

40 N. Fijoł, H. N. Abdelhamid, B. Pillai, S. A. Hall, N. Thomas and A. P. Mathew, 3D-Printed Monolithic Biofilters Based on a Polylactic Acid (PLA) – Hydroxyapatite (HAp) Composite for Heavy Metal Removal from an Aqueous Medium, *RSC Adv.*, 2021, **11**(51), 32408–32418, DOI: 10.1039/D1RA05202K.

41 S. Sultan, H. N. Abdelhamid, X. Zou and A. P. Mathew, CelloMOF: Nanocellulose Enabled 3D Printing of Metal-Organic Frameworks, *Adv. Funct. Mater.*, 2018, 1805372, DOI: 10.1002/adfm.201805372.

42 S. Bolisetty, M. Peydayesh and R. Mezzenga, Sustainable Technologies for Water Purification from Heavy Metals: Review and Analysis, *Chem. Soc. Rev.*, 2019, **48**(2), 463–487, DOI: 10.1039/C8CS00493E.

43 H. N. Abdelhamid, D. Georgouvelas, U. Edlund and A. P. Mathew, CelloZIFPaper: Cellulose-ZIF Hybrid Paper for Heavy Metal Removal and Electrochemical Sensing, *Chem. Eng. J.*, 2022, 136614, DOI: 10.1016/j.cej.2022.136614.

44 A. F. Abdel-Magied, H. N. Abdelhamid, R. M. Ashour, L. Fu, M. Dowaidar, W. Xia and K. Forsberg, Magnetic Metal-Organic Frameworks for Efficient Removal of Cadmium(II), and Lead(II) from Aqueous Solution, *J. Environ. Chem. Eng.*, 2022, 107467, DOI: 10.1016/j.jece.2022.107467.

45 H. N. Abdelhamid and A. Mathew, Cellulose-Metal Organic Frameworks (CelloMOFs) Hybrid Materials and Their Multifaceted Applications: A Review, *Coord. Chem. Rev.*, 2022, **451**, 214263, DOI: 10.1016/j.ccr.2021.214263.

46 H. N. Abdelhamid and H.-F. Wu, Reduced Graphene Oxide Conjugate Thymine as a New Probe for Ultrasensitive and Selective Fluorometric Determination of Mercury(II) Ions, *Microchim. Acta*, 2015, **182**(9–10), 1609–1617, DOI: 10.1007/s00604-015-1461-4.

47 H. N. Abdelhamid, J. Gopal and H.-F. F. Wu, Synthesis and Application of Ionic Liquid Matrices (ILMs) for Effective Pathogenic Bacteria Analysis in Matrix Assisted Laser Desorption/Ionization (MALDI-MS), *Anal. Chim. Acta*, 2013, **767**(1), 104–111, DOI: 10.1016/j.aca.2012.12.054.

48 H. N. Abdelhamid and H.-F. Wu, Ultrasensitive, Rapid, and Selective Detection of Mercury Using Graphene Assisted Laser Desorption/Ionization Mass Spectrometry, *J. Am. Soc. Mass Spectrom.*, 2014, **25**(5), 861–868, DOI: 10.1007/s13361-014-0825-z.

49 H. N. Abdelhamid, A. Talib and H. F. Wu, One Pot Synthesis of Gold – Carbon Dots Nanocomposite and Its Application for Cytosensing of Metals for Cancer Cells, *Talanta*, 2017, **166**, 357–363, DOI: 10.1016/j.talanta.2016.11.030.

50 R. Lindsey, Climate Change: Atmospheric Carbon Dioxide https://www.climate.gov/news-features/understanding-climate/climate-change-atmospheric-carbon-dioxide.

51 D. S. Goll, P. Ciais, T. Amann, W. Buermann, J. Chang, S. Eker, J. Hartmann, I. Janssens, W. Li, M. Obersteiner, J. Penuelas, K. Tanaka and S. Vicca, Potential CO_2 Removal from Enhanced Weathering by Ecosystem Responses to Powdered Rock, *Nat. Geosci.*, 2021, **14**(8), 545–549, DOI: 10.1038/s41561-021-00798-x.

52 H. N. Abdelhamid, Removal of Carbon Dioxide Using Zeolitic Imidazolate Frameworks: Adsorption and

Conversion via Catalysis, *Appl. Organomet. Chem.*, 2022, **36**(8), e6753, DOI: 10.1002/aoc.6753.

53 F. E.-Z. A. Abd El-Aziz, N. E. Ebrahem and H. N. Abdelhamid, A Comparative Study of the Toxic Effect of ZIF-8 and ZIF-L on the Colonization and Decomposition of Shaded Outdoor Mice Carrions by Arthropods, *Sci. Rep.*, 2022, **12**(1), 14240, DOI: 10.1038/s41598-022-18322-5.

54 H. N. Abdelhamid, Zeolitic Imidazolate Frameworks (ZIF–8, ZIF–67, and ZIF–L) for Hydrogen Production, *Appl. Organomet. Chem.*, 2021, **35**(9), e6319, DOI: 10.1002/aoc.6319.

55 H. Nasser Abdelhamid and A. P. Mathew, Cellulose-Zeolitic Imidazolate Frameworks (CelloZIFs) for Multifunctional Environmental Remediation: Adsorption and Catalytic Degradation, *Chem. Eng. J.*, 2021, **426**, 131733, DOI: 10.1016/j.cej.2021.131733.

56 O. Halevi, J. M. R. Tan, P. S. Lee and S. Magdassi, Hydrolytically Stable MOF in 3D-Printed Structures, *Adv. Sustainable Syst.*, 2018, **2**(2), 1700150, DOI: 10.1002/adsu.201700150.

57 C. A. Grande, R. Blom, V. Middelkoop, D. Matras, A. Vamvakeros, S. D. M. Jacques, A. M. Beale, M. Di Michiel, A. Andreassen, K. Bouzga and A. M, Multiscale Investigation of Adsorption Properties of Novel 3D Printed UTSA-16 Structures, *Chem. Eng. J.*, 2020, **402**, 126166, DOI: 10.1016/j.cej.2020.126166.

58 A. I. Cherevko, I. A. Nikovskiy, Y. V. Nelyubina, K. M. Skupov, N. N. Efimov and V. V. Novikov, 3D-Printed Porous Magnetic Carbon Materials Derived from Metal–Organic Frameworks, *Polymers*, 2021, **13**(22), 3881, DOI: 10.3390/polym13223881.

59 R. Chen, J. Yao, Q. Gu, S. Smeets, C. Baerlocher, H. Gu, D. Zhu, W. Morris, O. M. Yaghi and H. Wang, A Two-Dimensional Zeolitic Imidazolate Framework with a Cushion-Shaped Cavity for CO2 Adsorption, *Chem. Commun.*, 2013, **49**(82), 9500–9502, DOI: 10.1039/c3cc44342f.

